A Tight Correlation between Millimeter and X-Ray Emission in Accreting Massive Black Holes from <100 mas Resolution ALMA Observations

The Astrophysical Journal Letters, 952:L28 (7pp), 2023 August 1 https://doi.org/10.3847/2041-8213/acda27

A Tight Correlation between Millimeter and X-Ray Emission in Accreting Massive Black Holes from <100 mas Resolution ALMA Observations

Claudio Ricci[1,2], Chin-Shin Chang[3], Taiki Kawamuro[4], George C. Privon[5,6,7], Richard Mushotzky[8,9], Benny Trakhtenbrot[10], Ari Laor[11], Michael J. Koss[12,13], Krista L. Smith[14], Kriti K. Gupta[1], Georgios Dimopoulos[1], Susanne Aalto[15], and Eduardo Ros[16]

[1] Instituto de Estudios Astrofísicos, Facultad de Ingeniería y Ciencias, Universidad Diego Portales, Av. Ejército Libertador 441, Santiago, Chile; claudio.ricci@mail.udp.cl
[2] Kavli Institute for Astronomy and Astrophysics, Peking University, Beijing 100871, People's Republic of China
[3] Joint ALMA Observatory, Avenida Alonso de Cordova 3107, Vitacura 7630355, Santiago, Chile
[4] RIKEN Cluster for Pioneering Research, 2-1 Hirosawa, Wako, Saitama 351-0198, Japan
[5] National Radio Astronomy Observatory, 520 Edgemont Road, Charlottesville, VA 22903, USA
[6] Department of Astronomy, University of Florida, P.O. Box 112055, Gainesville, FL 32611, USA
[7] Department of Astronomy, University of Virginia, 530 McCormick Road, Charlottesville, VA 22904, USA
[8] Department of Astronomy, University of Maryland, College Park, MD 20742, USA
[9] Joint Space-Science Institute, University of Maryland, College Park, MD 20742, USA
[10] School of Physics and Astronomy, Tel Aviv University, Tel Aviv 69978, Israel
[11] Physics Department, Technion, Haifa 32000, Israel
[12] Eureka Scientific, 2452 Delmer Street Suite 100, Oakland, CA 94602-3017, USA
[13] Space Science Institute, 4750 Walnut Street, Suite 205, Boulder, CO 80301, USA
[14] Southern Methodist University, Department of Physics, Dallas, TX 75205, USA
[15] Department of Space, Earth and Environment, Onsala Space Observatory, Chalmers University of Technology, Onsala, Sweden
[16] Max-Planck-Institut für Radioastronomie, Auf dem Hügel 69, D-53121, Bonn, Germany
Received 2023 May 23; accepted 2023 May 30; published 2023 July 26

Abstract

Recent studies have proposed that the nuclear millimeter continuum emission observed in nearby active galactic nuclei (AGNs) could be created by the same population of electrons that gives rise to the X-ray emission that is ubiquitously observed in accreting black holes. We present the results of a dedicated high-spatial-resolution (∼60–100 mas) Atacama Large Millimeter/submillimeter Array (ALMA) campaign on a volume-limited (<50 Mpc) sample of 26 hard X-ray (>10 keV) selected radio-quiet AGNs. We find an extremely high detection rate (25/26 or 94^{+3}_{-6}%), which shows that nuclear emission at millimeter wavelengths is nearly ubiquitous in accreting SMBHs. Our high-resolution observations show a tight correlation between the nuclear (1–23 pc) 100 GHz and the intrinsic X-ray emission (1σ scatter of 0.22 dex). The ratio between the 100 GHz continuum and the X-ray emission does not show any correlation with column density, black hole mass, Eddington ratio, or star formation rate, which suggests that the 100 GHz emission can be used as a proxy of SMBH accretion over a very broad range of these parameters. The strong correlation between 100 GHz and X-ray emission in radio-quiet AGNs could be used to estimate the column density based on the ratio between the observed 2–10 keV ($F^{\rm obs}_{2-10\,{\rm keV}}$) and 100 GHz ($F_{100\,{\rm GHz}}$) fluxes. Specifically, a ratio $\log(F^{\rm obs}_{2-10\,{\rm keV}}/F_{100\,{\rm GHz}}) \leqslant 3.5$ strongly suggests that a source is heavily obscured ($\log(N_{\rm H}/{\rm cm}^{-2}) \gtrsim 23.8$). Our work shows the potential of ALMA continuum observations to detect heavily obscured AGNs (up to an optical depth of one at 100 GHz, i.e., $N_{\rm H} \simeq 10^{27}\,{\rm cm}^{-2}$), and to identify binary SMBHs with separations <100 pc, which cannot be probed by current X-ray facilities.

Unified Astronomy Thesaurus concepts: Active galactic nuclei (16); X-ray active galactic nuclei (2035); Supermassive black holes (1663)

1. Introduction

The vast majority (∼90%) of active galactic nuclei (AGNs) emit only only faintly in the radio, and are therefore usually referred to as radio-quiet (e.g., Wilson & Colbert 1995). These objects typically do not show the prominent jets observed in radio-loud AGNs (Begelman et al. 1984; Zensus 1997). Radio emission is, however, detected almost ubiquitously in these radio-quiet AGNs, and in many cases is unresolved and comes from a very compact, subkiloparsec nuclear region (e.g., Panessa et al. 2019; Smith et al. 2020, and references therein). Similarly, studies carried out in the millimeter regime have shown the presence of a prominent nuclear emission component in radio-quiet AGNs (e.g., Behar et al. 2015; Kawamuro et al. 2022). It has been argued that this component might be associated with the same region that produces the X-ray radiation universally observed in AGNs (e.g., Laor & Behar 2008; Inoue & Doi 2014; Doi & Inoue 2016; Panessa et al. 2019; Kawamuro et al. 2022): the so-called X-ray corona.

The electrons in the corona up-scatter optical/UV photons produced in the accretion flow into the X-ray band. The heating mechanism of the corona is still debated, but it has been widely suggested that magnetic reconnection could play an important role (e.g., Galeev et al. 1979; Di Matteo et al. 1997; Merloni & Fabian 2001a, 2001b). The magnetized corona is expected to generate cyclo/synchrotron radiation, observable in the radio/millimeter band (e.g., Laor & Behar 2008; Inoue & Doi 2014; Panessa et al. 2019). X-ray reverberation studies

(e.g., Fabian et al. 2009; Emmanoulopoulos et al. 2011; De Marco et al. 2013; Uttley et al. 2014; Kara et al. 2016; Cackett et al. 2021) have shown that the X-ray corona is located at a few gravitational radii[17] from the supermassive black hole (SMBH). The size of the corona has been found to be relatively small (5–10 R_g) from rapid X-ray variability (e.g., McHardy et al. 2005), X-ray eclipses (e.g., Risaliti et al. 2007), and microlensing studies (e.g., Chartas et al. 2009). Coming from a compact region close to the SMBH, the coronal millimeter-wave synchrotron emission is expected to be self-absorbed, and it would therefore be more easily detectable in the millimeter than in the radio. The size (R) of a self-absorbed synchrotron source decreases with the frequency following $R \propto \nu^{-7/4}$, implying that the synchrotron emission from an X-ray corona sized source would peak at ∼100 GHz. Several studies have indeed shown that the fluxes at 100 GHz systematically exceed the extrapolation of the low-frequency steep slope power law (e.g., Behar et al. 2015; Doi & Inoue 2016; Behar et al. 2018; Inoue & Doi 2018). Moreover, some models (e.g., Raginski & Laor 2016; Inoue & Doi 2018) suggest that the coronal emission could produce flat synchrotron emission up to ≈300 GHz. This was recently corroborated by the observational study of Kawamuro et al. (2022), which found the millimeter-wave nuclear emission in their AGN sample to be spectrally flat at ∼230 GHz, with spectral slopes[18] of $\alpha_\nu \sim 0.5$, inconsistent with what would be expected from thermal dust ($\alpha \sim -3.5$).

A coronal origin for the millimeter continuum would produce a tight correlation between the continuum emission in the X-ray and the ∼100–200 GHz bands. Studying eight radio-quiet AGNs observed by CARMA, Behar et al. (2015) found a correlation between the 95 GHz and 2–10 keV luminosities. However, expanding the sample to 26 objects, Behar et al. (2018) found a large scatter in this correlation, likely due to the heterogeneity of the sample and of the physical scales probed, as well as to the low angular resolution of the millimeter data ($\gtrsim 1''$). Using higher-resolution ($<1''$ or <200 pc) Atacama Large Millimeter/submillimeter Array (ALMA) 230 GHz observations of 98 nearby AGNs, Kawamuro et al. (2022) found a tighter correlation between these two bands, with a typical scatter of ∼0.35 dex. The average ratio between the ∼100–200 GHz and X-ray continuum is $\sim 10^{-4}$ (Behar et al. 2015, 2018; Kawamuro et al. 2022). Interestingly, this relation is consistent with what has been observed in coronally active stars (Guedel & Benz 1993), which are magnetically heated, similarly to what is expected for AGN coronae, further supporting the idea of a coronal origin for the 100–200 GHz continuum emission. However, about 50% of the AGNs in the study of Kawamuro et al. (2022) showed weak resolved emission at 230 GHz, which potentially contaminates the nuclear emission and complicates its interpretation.

With the goal of probing smaller scales in a homogeneous way, we study here the relation between X-ray and 100 GHz emission using the results obtained by a dedicated very-high-resolution (<100 mas) ALMA campaign of a volume-limited ($D < 50$ Mpc) sample of hard X-ray (>10 keV) selected radio-quiet AGNs. Our observations probe physical scales between 1.5 and 23 pc. Our sample covers a large range in column density, black hole masses, X-ray luminosities, Eddington ratios, and star formation rates. Throughout the paper we adopt standard cosmological parameters ($H_0 = 70$ km s^{-1} Mpc^{-1}, $\Omega_m = 0.3$, $\Omega_\Lambda = 0.7$).

2. Sample

The Burst Alert Telescope (BAT) instrument on board the Swift satellite has detected over 1000 nearby AGNs ($z < 0.1$) in the 14–195 keV range (Baumgartner et al. 2013; Oh et al. 2018). This energy band is not affected by obscuration up to column densities of $\sim 10^{24}$ cm^{-2}, which has allowed BAT to detect and identify a significant number of heavily obscured, previously unknown AGNs (e.g., Ricci et al. 2015). Swift/BAT also probes a luminosity range consistent to that of the bulk of the AGN population at higher redshifts ($z \sim 1$–4; see Figure 5 of Koss et al. 2017). The sources of our sample are part of the BAT AGN Spectroscopic Survey[19] (BASS; Ricci et al. 2017a; Koss et al. 2017, 2022b), that is measuring the optical spectra and multiwavelength properties of this minimally biased sample of nearby AGNs, with the goal of creating the benchmark of SMBH accretion at low redshifts. BASS provides accurate measurements of redshifts, X-ray luminosities, column densities, black hole masses (M_{BH}), and Eddington ratios (λ_{Edd}).

Our sample was drawn from the Swift/BAT 70 month catalog (Baumgartner et al. 2013). We included all the radio-quiet AGNs within 50 Mpc with a decl. <10° (i.e., accessible by ALMA). Radio-loudness was estimated using the ratio between the archival 1.4 GHz luminosity and the intrinsic 14–195 keV X-ray luminosity ($R_X = L_{1.4GHz}/L_{14-195\,keV}$), following Teng et al. (2011; see also Terashima & Wilson 2003). Consistently with these studies, radio-quiet AGNs were defined as those with $\log R_X \leqslant -4.7$. We note that most of the sources in our sample actually have $\log R_X \leqslant -5.2$, well below our radio-quiet limit. For the six sources for which no archival 1.4 GHz fluxes were available we used a similar approach, considering either the 4.85 GHz or the 843 MHz fluxes, to verify that the sources were radio-quiet. Our final sample consists of 26 objects, of which eight are unobscured ($N_H < 10^{22}$ cm^{-2}), 10 are obscured by Compton-thin material ($10^{22} \leqslant N_H < 10^{24}$ cm^{-2}), and eight are obscured by Compton-thick (CT) gas ($N_H \geqslant 10^{24}$ cm^{-2}). The sample is a very good representation of the intrinsic column density distribution of nearby AGNs (i.e., corrected for selection biases; e.g., Ricci et al. 2015, 2017b, 2022), and it covers a broad range of 14–150 keV luminosities [$41.5 \leqslant \log(L_{14-150}/\mathrm{erg\ s^{-1}}) \leqslant 44$], black hole masses ([$6 \leqslant \log(M_{BH}/M_\odot) \leqslant 9$], and Eddington ratios ($-3 \leqslant \log\lambda_{Edd} \leqslant 0$).

We use the X-ray fluxes and column densities obtained by Ricci et al. (2017a) through broadband (0.3–150 keV) X-ray spectral analysis. For the eight CT sources, we included more recent NuSTAR data to obtain a more accurate estimate of their intrinsic fluxes. We use the black hole masses reported in the second data release of BASS (Koss et al. 2022a, 2022c; Mejía-Restrepo et al. 2022). For the eight CT AGNs, we estimated the Eddington ratios considering the intrinsic X-ray luminosity obtained by our new X-ray spectroscopic analysis (i.e., including the new NuSTAR data). This was done using the same X-ray spectral models outlined in Ricci et al. (2017a). For NGC 5643 we used the results of the detailed study carried out by Annuar et al. (2015), which used a similar spectral decomposition approach. All luminosities were calculated

[17] $R_g = GM_{BH}/c^2$ is the gravitational radius for an SMBH of mass M_{BH}.
[18] Considering $F_\nu \propto \nu^{-\alpha_\nu}$.
[19] http://bass-survey.com

using the distances reported in Koss et al. (2022a), which include redshift-independent distance measurements for several of these nearby AGNs. Bolometric luminosities ($L_{\rm Bol}$) were calculated considering a uniform 14–150 keV bolometric correction of $\kappa_{14-150} = 8.48$ ($L_{\rm Bol} = \kappa_{14-150} \times L_{14-150}$), equivalent to a 2–10 keV bolometric correction of $\kappa_{2-10} = 20$ (Vasudevan & Fabian 2009) for the median X-ray photon index of nearby AGNs ($\Gamma = 1.8$, Ricci et al. 2017a). The Eddington ratios ($\lambda_{\rm Edd} = L_{\rm Bol}/L_{\rm Edd}$) were estimated by calculating the Eddington luminosity $L_{\rm Edd} = \frac{4\pi G M_{\rm BH} m_{\rm p} c}{\sigma_{\rm T}}$, where G is the gravitational constant, $M_{\rm BH}$ is the black hole mass, $m_{\rm p}$ is the mass of the proton, c is the speed of light, and $\sigma_{\rm T}$ is the Thomson cross section.

3. ALMA Data Reduction

The 100 GHz fluxes were obtained by a dedicated ALMA campaign (2019.1.01230.S; PI: C. Ricci) with ∼60–100 mas resolution. We report here some basic details of our analysis. A detailed description of the ALMA analysis will be reported in a forthcoming paper (C. S. Chang et al. 2023, in preparation), which will also focus on a second ALMA campaign, that observed the same objects with lower (0.″2 to 0.″3) resolution. The band-3 ALMA data were calibrated and imaged using ALMA pipeline version 2020.1.0.40 and the Common Astronomy Software Applications (CASA) version 6.1.1.15. Briggs weighting with robust parameter equal to 0.5 is used for the imaging of all the sources, with a little loss in sensitivity from robust = 2.0, which yields the possible lowest noise level, allowing us to retain almost the highest resolution. The corresponding aggregated continuum maps, and the images of the four spectral windows are created, and the primary-beam corrections are applied. For each source, the peak flux of the aggregated continuum map is used for this study. In two cases (NGC 3281 and NGC 4941) ALMA detected two nuclear sources (per galaxy), separated by ∼0.″3. In both cases, the fluxes of the two nuclear sources were almost identical, with flux ratios of 1.07 and 1.11 for NGC 4941 and NGC 3281, respectively. For the present analysis, we used only the brighter source in each of these two systems, but we stress that this choice does not significantly change our results. Only in one case (MCG−05−14−012), ALMA did not detect any source at the location of the AGN, and we only report the 3σ upper limit on 100 GHz flux and luminosity. This is likely due to the low flux of the source, as the 14–150 keV flux of MCG−05−14−012 is in fact the second lowest in the sample (17.9×10^{-12} erg^{-1} s^{-1} cm^{-2}). Interestingly, this source was also not detected by ALMA at 200 GHz (Kawamuro et al. 2022). We checked whether the ALMA nondetection could be ascribed to variability, and found that a NuSTAR observation carried out ∼3 weeks before the ALMA observation (ID 60160243002) points toward the same 14–150 keV flux reported by Ricci et al. (2017a; $\log(F_{14-150\,\rm keV}/\,{\rm erg^{-1}\,s^{-1}\,cm^{-2}}) = -10.75$). This seems to rule out variability as the main cause of the ALMA nondetection. The 100 GHz emission in all other objects is dominated by an unresolved nuclear component. The sources in our sample, together with their distances, column densities, 100 GHz and 14–150 keV fluxes and luminosities, are listed in Table 1.

4. The Relation between X-Ray and 100 GHz Emission

Our sensitive 100 GHz ALMA observations detect a very high fraction (25/26 or 94^{+3}_{-6}%) of the radio-quiet AGNs of our sample, showing that an unresolved core at millimeter wavelengths is almost ubiquitous in accreting SMBHs. Interestingly, a similar detection fraction was obtained for BAT AGN at 22GHz by lower-resolution (1″) observations (Smith 2016). In the left panel of Figure 1, we show the relation between the 100 GHz continuum luminosity obtained through our high-resolution ALMA observations and the intrinsic 14–150 keV luminosities from Ricci et al. (2017a). These X-ray luminosities were integrated over a period of 70 months of BAT observations, and are therefore a good measure of the average AGN X-ray emission. The figure shows a very clear positive correlation between the X-ray and the 100 GHz luminosity. The correlation is very significant, with a p-value $\lesssim 10^{-5}$. Given the very tight correlation between the 100 GHz and the X-ray emission, the former could be used as a proxy for the AGN power.

Fitting the logarithms of the luminosities (in erg s^{-1}) with a linear relation, using a standard linear least-squares method, we obtain

$$\log L_{100\,\rm GHz} = (-14.4 \pm 0.8) + (1.22 \pm 0.02) \log L_{14-150\,\rm keV}, \quad (1)$$

which is shown as a red solid line in the left panel of Figure 1. The 1σ scatter of the correlation is ≃0.22 dex. Interestingly the slope and scatter are consistent with what was found by Kawamuro et al. (2022) for the 230 GHz emission of a subsample of radio-quiet AGNs ($1.19^{+0.08}_{-0.05}$ and 0.23 dex, respectively).

A tight correlation is also obtained when using the 100 GHz and 14–195 keV fluxes (in erg s^{-1} cm^{-2}; right panel of Figure 1), with the same 1σ scatter (0.22 dex). The best-fit relation is

$$\log F_{100\,\rm GHz} = (-1.3 \pm 0.4) + (1.37 \pm 0.04) \log F_{14-150\,\rm keV}. \quad (2)$$

It should be noticed that, at least part of the scatter could be due to variability, since the 100 GHz and X-ray observations are not simultaneous. Interestingly, it has been argued, by analyzing the typical cross-correlation constants obtained by fitting time-averaged Swift/BAT and short Swift/XRT, XMM-Newton/EPIC and Suzaku/XIS observations, that on timescales of days to several years the X-ray variability of nonblazar AGNs is ∼0.2 dex (Ricci et al. 2017a).

The 2–10 keV band is commonly used in AGN surveys and studies, making it perhaps a more useful proxy of AGN coronal emission. In order to obtain the relation between 100 GHz and 2–10 keV emission, we first converted the 14–150 keV fluxes and luminosities to the 2–10 keV band assuming a pure power-law spectral model with a photon index $\Gamma = 1.8$ (Ricci et al. 2017a). This was done to consider the average 2–10 keV emission for these objects. We then obtained a best-fit relation for the luminosities of the form

$$\log L_{100\,\rm GHz} = (-13.9 \pm 0.8) + (1.22 \pm 0.02) \log L_{2-10\,\rm keV}, \quad (3)$$

while for the fluxes we obtained

$$\log F_{100\,\rm GHz} = (0.6 \pm 0.4) + (1.37 \pm .04) \log F_{2-10\,\rm keV}. \quad (4)$$

The typical ratio between the 100 GHz continuum and the 14–150 keV (2–10 keV) emission is $\log(L_{100\,\rm GHz}/L_{14-150\,\rm keV}) = -5.00 \pm 0.06$ ($\log(L_{100\,\rm GHz}/L_{2-10\,\rm keV}) = -4.63 \pm 0.06$).

We further looked for possible links between the X-ray–to–millimeter correlation and several other key AGN quantities. Specifically, we looked at the ratio between the

Table 1
List of SWIFT/BAT AGNs Used in This Study (See Section 2 for Details on the Sample Selection)

(1) SWIFT ID	(2) Counterpart	(3) Distance (Mpc)	(4) $\log N_{\rm H}$ ($\rm cm^{-2}$)	(5) $\log F_{100\,\rm GHz}$ ($\rm erg\,s^{-1}\,cm^{-2}$)	(6) $\log F_{14-150\,\rm keV}$ ($\rm erg\,s^{-1}\,cm^{-2}$)	(7) $\log L_{100\,\rm GHz}$ ($\rm erg\,s^{-1}$)	(8) $\log L_{14-150\,\rm keV}$ ($\rm erg\,s^{-1}$)
SWIFT J0251.6−1639	NGC 1125	48.0	24.45	−15.40	−10.33	38.04	43.11
SWIFT J0543.9−2749	MCG−05−14−012	41.9	20.00	$\leqslant -16.22$	−10.75	$\leqslant$37.10	42.57
SWIFT J0552.2−0727	NGC 2110	34.3	22.94	−14.25	−9.55	38.89	43.59
SWIFT J0601.9−8636	ESO 5−4	28.2	24.29	−15.72	−10.39	37.25	42.59
SWIFT J0947.6−3057	MCG−5−23−16	36.2	22.18	−14.38	−9.76	38.81	43.44
SWIFT J0959.5−2248	NGC 3081	32.5	23.91	−15.20	−9.92	37.90	43.18
SWIFT J1023.5+1952	NGC 3227	23.0	20.95	−15.07	−10.03	37.73	42.77
SWIFT J1031.7−3451	NGC 3281	48.1	23.98	−14.95	−9.99	38.49	43.45
SWIFT J1139.0−3743	NGC 3783	38.5	20.49	−14.67	−9.80	38.58	43.45
SWIFT J1212.9+0702	NGC 4180	43.1	24.28	−15.82	−10.73	37.52	42.61
SWIFT J1225.8+1240	NGC 4388	18.1	23.52	−14.80	−9.55	37.80	43.05
SWIFT J1239.6−0519	NGC 4593	37.2	20.00	−14.91	−10.12	38.31	43.10
SWIFT J1304.3−0532	NGC 4941	20.5	23.72	−15.72	−10.71	36.98	41.98
SWIFT J1305.4−4928	NGC 4945	3.5	24.60	−14.09	−9.53	37.07	41.63
SWIFT J1332.0−7754	ESO 21−4	41.6	23.80	−15.20	−10.69	38.11	42.63
SWIFT J1335.8−3416	MCG−6−30−15	30.4	20.85	−15.22	−10.27	37.82	42.78
SWIFT J1432.8−4412	NGC 5643	12.7	24.56	−14.99	−10.04	37.29	42.25
SWIFT J1442.5−1715	NGC 5728	37.5	24.16	−14.83	−9.84	38.40	43.38
SWIFT J1635.0−5804	ESO 137−34	34.1	24.32	−15.46	−10.42	37.69	42.72
SWIFT J1652.0−5915A	ESO 138−1	39.3	25.00	−14.85	−9.46	38.41	43.81
SWIFT J1652.0−5915B	NGC 6221	11.9	21.15	−15.49	−10.74	36.73	41.48
SWIFT J1717.1−6249	NGC 6300	13.2	23.31	−15.11	−10.03	37.21	42.29
SWIFT J1942.6−1024	NGC 6814	22.8	20.97	−15.32	−10.18	37.48	42.61
SWIFT J2035.6−5013	Fairall 346	37.7	23.08	−15.37	−11.00	37.86	42.22
SWIFT J2201.9−3152	NGC 7172	33.9	22.91	−15.05	−9.96	38.09	43.17
SWIFT J2235.9−2602	NGC 7314	16.8	21.60	−15.43	−10.37	37.10	42.15

Note. The table reports the sources names (1, 2), their distance (3), column density (4), fluxes (5, 6), and luminosities (7, 8) in the 100 GHz and 14–150 keV bands.

X-ray–to–100 GHz continuum luminosity versus the column density (top left panel of Figure 2), Eddington ratio (top right panel), and black hole mass (bottom left panel). We also checked how this ratio varies with star formation rate of the host galaxy (bottom right panel of Figure 2), inferred through IR spectral energy distribution decomposition by Ichikawa et al. (2017, 2019). In all cases we found no statistically significant trend in the X-ray–to–100 GHz ratio. This shows that the relations reported in Equations (1)–(4) is applicable over a wide range of AGN/SMBH and host properties. Moreover, this analysis provides further insight regarding the origin of the 100 GHz emission. As discussed in Kawamuro et al. (2022), if the 100 GHz emission was due to outflow-driven shocks, then one might expect an increase in $L_{100\,\rm GHz}/L_{14-150\,\rm keV}$ with increasing $\lambda_{\rm Edd}$, which is not observed here (top right panel of Figure 2).

5. Estimating Column Densities from the X-Ray–100 GHz Relation

The tight correlation between 100 GHz continuum and the intrinsic X-ray emission could be used to infer the column density of heavily obscured objects, which are either only faintly detected in the X-rays or show a heavily obscured X-ray spectrum. Considering that 20%–30% of all AGNs are obscured by material with $\log(N_{\rm H}/\rm cm^{-2}) \gtrsim 24$ (e.g., Burlon et al. 2011; Ricci et al. 2015; Torres-Albà et al. 2021), any independent approach to detect and survey them would clearly be very useful. Radiation at 100 GHz can penetrate large columns of gas, even more than the hard X-ray emission, which is strongly affected by obscuration above $10^{24}\,\rm cm^{-2}$ (see Figure 1 of Ricci et al. 2015). According to Hildebrand (1983), the extinction at ∼100 GHz is $N_{\rm H}/\tau = 1.2 \times 10^{25} \times (\lambda/400\,\mu\rm m)^2$, which implies that the material becomes optically thick at 100 GHz only at $\approx 10^{27}\,\rm cm^{-2}$, i.e., ∼3 orders of magnitude above the optically thick limit for the hard X-ray band. Therefore, our calibration of the relation between the 100 GHz and X-ray luminosities would allow us to use the nuclear 100 GHz flux as a proxy of the intrinsic power of AGNs, and the ratio between millimeter and X-ray observed fluxes to estimate absorbing column densities.

In Figure 3 we show the ratio between the observed 2–10 keV and 100 GHz fluxes and how it varies with column density for the objects of our sample. As expected, for increasing $N_{\rm H}$ the ratio decreases, due to the increasing effect of obscuration on the observed 2–10 keV AGN emission. The green dot-dotted–dashed line in the figure shows the expected decrease of the flux ratio with column density by considering an X-ray spectral model typical of obscured AGNs. This was done by using the REFLEX (Paltani & Ricci 2017) model RXTORUSD, the first torus X-ray spectral model that includes dusty gas (Ricci & Paltani 2023). The photon index and cutoff energy of the primary continuum in this model were set to the median values of AGNs in the local universe (Ricci et al. 2017a), i.e., $\Gamma = 1.8$ and $E_{\rm C} = 200\,\rm keV$, respectively. The model includes absorbed and reprocessed radiation from a torus covering 70% of the X-ray source, plus an unobscured Thomson scattered component with a scattered fraction of $f_{\rm scatt} = 1.1\%$, which is expected to be created by material located on scales >10–100 pc from the SMBH (e.g., Bianchi et al. 2006). The latter component is responsible for the

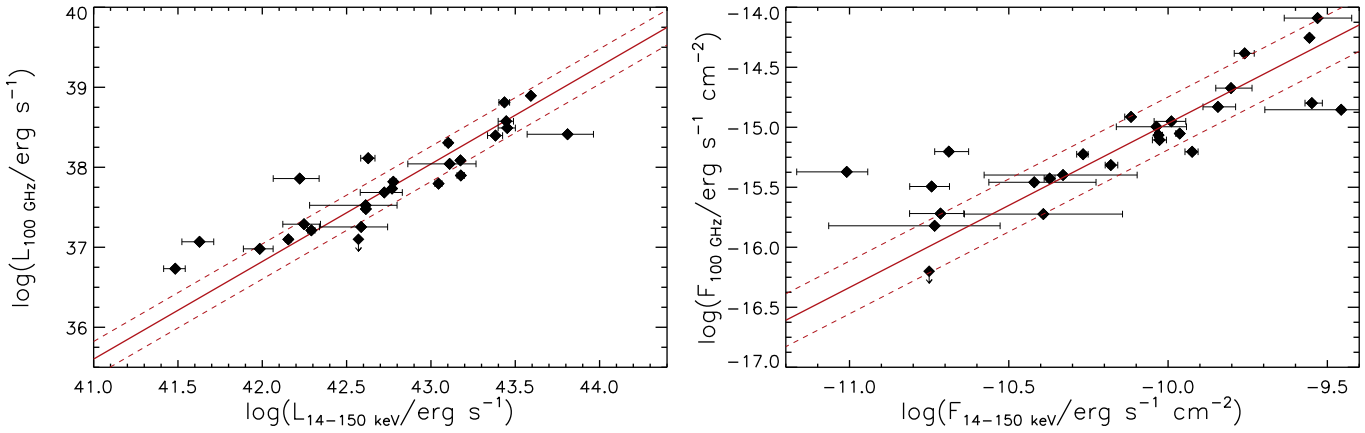

Figure 1. Left panel: 100 GHz continuum luminosity vs. the intrinsic 14–150 keV luminosity for the sources in our sample. The solid red line represents the best fit to the data (Equation (1)), while the dashed red lines show the 1σ scatter (0.22 dex). Right panel: same but for the corresponding fluxes (best-fit relation given in Equation (2)). Uncertainties on the ALMA 100 GHz fluxes and luminosities are 5%.

flattening of the curve for $\log(N_{\rm H}/{\rm cm}^{-2}) \gtrsim 24.5$. It should be stressed that the behavior of the curve for high column densities (and in particular its flattening) is significantly influenced by the choice of covering factor and scattered fraction values. A recent study focused on nearby AGNs has shown that $f_{\rm scatt}$ significantly declines for increasing column densities (Gupta et al. 2021), which would lead to lower values of $F^{\rm obs}_{2-10\,{\rm keV}}/F_{100{\rm GHz}}$ for $\log(N_{\rm H}/{\rm cm}^{-2}) \gtrsim 24.5$.

We fit our data in the $\log(N_{\rm H}/{\rm cm}^{-2}) = 22 - 24.5$ interval and find that, in this range, $N_{\rm H}$ can be inferred from the ratio between the observed 2–10 keV and the 100 GHz fluxes ($F^{\rm obs}_{2-10\,{\rm keV}}/F_{100\,{\rm GHz}}$) using the relation

$$\log \frac{N_{\rm H}}{{\rm cm}^{-2}} = (28.2 \pm 0.2) + (-1.30 \pm 0.05) \log \frac{F^{\rm obs}_{2-10\,{\rm keV}}}{F_{100\,{\rm GHz}}}, \quad (5)$$

which is shown as a red dashed line in Figure 3. We recommend to use this relation in the range $\log(F^{\rm obs}_{2-10\,{\rm keV}}/F_{100\,{\rm GHz}}) \simeq 2.7$–4.5, with $\log(F^{\rm obs}_{2-10\,{\rm keV}}/F_{100\,{\rm GHz}}) \lesssim 2.7$ typically implying $\log(N_{\rm H}/{\rm cm}^{-2}) \gtrsim 24.5$. On the other hand, $\log(F^{\rm obs}_{2-10\,{\rm keV}}/F_{100\,{\rm GHz}}) \gtrsim 4.5$ implies $\log(N_{\rm H}/{\rm cm}^{-2}) \lesssim 22.5$. In the figure for $\log(N_{\rm H}/{\rm cm}^{-2}) \gtrsim 24.5$ we assumed a constant value of $\log(F^{\rm obs}_{2-10\,{\rm keV}}/F_{100\,{\rm GHz}}) \simeq 2.7$, similarly to what was found by using the theoretical X-ray spectral model, although this value could change depending on the structure and properties of the obscuring material. The $F^{\rm obs}_{2-10\,{\rm keV}}/F_{100\,{\rm GHz}}$ ratio could be used to efficiently select obscured AGNs: from Figure 3 it is clear that, typically, $\log(F^{\rm obs}_{2-10\,{\rm keV}}/F_{100\,{\rm GHz}}) \leqslant 3.5$ would strongly suggest that the AGN is heavily obscured [$\log(N_{\rm H}/{\rm cm}^{-2}) \gtrsim 23.8$].

6. Summary and Conclusions

With the goal of constraining the relation between millimeter and X-ray continuum emission in AGNs, we have studied here a sample of 26 hard X-ray selected, radio-quiet AGNs at distances <50 Mpc with ALMA at <100 mas resolution (corresponding to 1.5–23 pc; see Section 2 for details). The sources were selected from the Swift/BAT 70 month catalog (Baumgartner et al. 2013), and have a large amount of ancillary data available (Ricci et al. 2017a; Ichikawa et al. 2017; Koss et al. 2022a). Our results are as follows:

1. Our sensitive 100 GHz ALMA observations detect a very high fraction (25/26 or 94^{+3}_{-6}%) of the radio-quiet AGNs of our sample, showing that an unresolved core at millimeter wavelengths is almost ubiquitous in accreting SMBHs.
2. Our observations indicate a very tight correlation between the 100 GHz and the intrinsic X-ray emission (Figure 1). The 1σ scatter between the fluxes (or luminosities) is merely 0.22 dex (Section 4). Considering that the 100 GHz and X-ray observations are not simultaneous, one would expect that the intrinsic scatter might be even smaller. The relations between the 100 GHz and X-ray luminosities and fluxes are reported in Equations (1)–(4).
3. The median ratio between the 100 GHz continuum and 14–150 keV (2–10 keV) emission is $\log(L_{100\,{\rm GHz}}/L_{14-150\,{\rm keV}}) = -5.00 \pm 0.06$ [$\log(L_{100\,{\rm GHz}}/L_{2-10\,{\rm keV}}) = -4.63 \pm 0.06$]. This ratio shows no correlation with column density, black hole mass, Eddington ratio, or star formation rate (Figure 2), which suggests that the 100 GHz emission can be used as a proxy of the intrinsic X-ray luminosity over a broad range of these parameters (Section 4).
4. The tight correlation between 100 GHz and X-ray emission could be used to infer the column density in radio-quiet AGNs. The value of $N_{\rm H}$ can be inferred from the ratio between the observed 2–10 keV and 100 GHz fluxes using Equation (5) for $\log(F^{\rm obs}_{2-10\,{\rm keV}}/F_{100\,{\rm GHz}}) \simeq$ 2.7–4.5 (see Figure 3). A value of $\log(F^{\rm obs}_{2-10\,{\rm keV}}/F_{100\,{\rm GHz}}) \lesssim 2.7$ typically suggests $\log(N_{\rm H}/{\rm cm}^{-2}) \gtrsim 24.5$, while $\log(F^{\rm obs}_{2-10\,{\rm keV}}/F_{100\,{\rm GHz}}) \gtrsim 4.5$ implies $\log(N_{\rm H}/{\rm cm}^{-2}) \lesssim$ 22.5. Generally $\log(F^{\rm obs}_{2-10\,{\rm keV}}/F_{100\,{\rm GHz}}) \leqslant 3.5$ strongly suggests that the source is heavily obscured ($\log(N_{\rm H}/{\rm cm}^{-2}) \gtrsim 23.8$; Section 5).

Our work shows that the nuclear 100 GHz emission could be used as a proxy of the intrinsic (bolometric) power of accreting SMBHs. ALMA continuum observations could be very useful to detect heavily obscured AGNs, even at $z \sim 1$–2, up to column densities of $\approx 10^{27}\,{\rm cm}^{-2}$, above which the 100 GHz emission is also significantly attenuated. Moreover, these millimeter observations can potentially reach spatial resolutions $\sim$10–20 times better than the best X-ray facilities (e.g., Chandra 0.″5), to identify close dual AGNs in the final phase

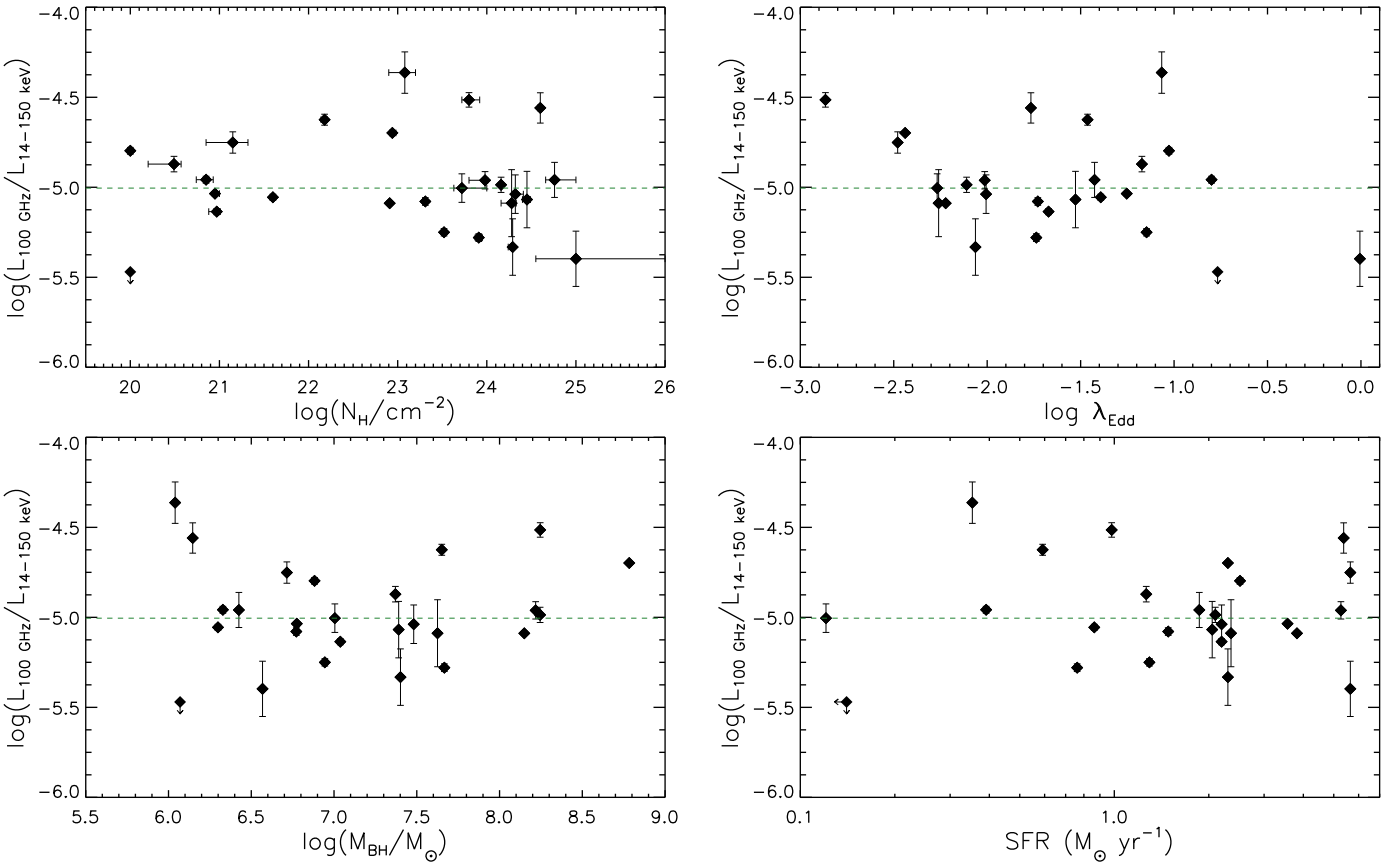

Figure 2. The ratio between 100 GHz and intrinsic 14–150 keV luminosities vs. the column density (top left panel), Eddington ratio (top right panel), black hole mass (bottom left panel), and star formation rate (bottom right panel). The horizontal dashed green lines represent the median value of $\log(L_{100\,\mathrm{GHz}}/L_{14-150\,\mathrm{keV}})$.

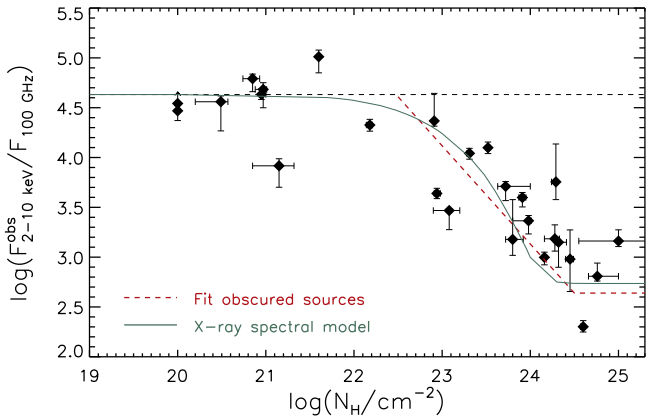

Figure 3. The ratio between the observed fluxes in the 2–10 keV and in the 100 GHz bands vs. the column density for the objects in our sample. The horizontal black dashed line marks the median value of the ratio obtained using the intrinsic 2–10 keV fluxes (see Section 4). The dashed red line represents the best fit to the data in the $\log(N_{\rm H}/{\rm cm}^{-2}) = 22-24.5$ range (see Equation (5)). The green dot-dotted–dashed line shows the expected decrease of the flux ratio with $N_{\rm H}$ by considering the RXTORUSD model.

of dynamical friction (e.g., $\lesssim$250 pc; Koss et al. 2023) and potentially even binary SMBHs ($\lesssim$100 pc).

However, it is still unclear what physical mechanisms produces the millimeter continuum in AGNs. It has been proposed that this emission might be produced by the X-ray corona (e.g., Laor & Behar 2008; Inoue & Doi 2014; Behar et al. 2018; Inoue & Doi 2018; Kawamuro et al. 2022). While the recent work of Kawamuro et al. (2022; focused on 230 GHz emission) showed that a dust origin for the millimeter emission appears unlikely, one cannot rule out that it is associated with shocks produced by outflows or to free–free emission in the inner regions of the AGN. However, the lack of a correlation between $\log(L^{\rm obs}_{2-10\,\mathrm{keV}}/L_{100\,\mathrm{GHz}})$ and $\lambda_{\rm Edd}$, found both here (Figure 2) and in Kawamuro et al. (2022), appears to argue against the millimeter emission being associated with shocks produced by outflows, at least for the Eddington ratio regime probed here ($\lambda_{\rm Edd} \simeq 10^{-3}$–$10^{-0.8}$). Future studies of millimeter variability, correlated millimeter and X-ray variability, as well as higher spatial resolution studies carried out with the Global 3 mm VLBI Array, will help shed light on the origin of the nuclear millimeter emission in AGNs and its relation to the X-ray corona.

Acknowledgments

C.R. acknowledges support from the Fondecyt Regular grant 1230345 and ANID BASAL project FB210003. B.T. acknowledges support from the European Research Council (ERC) under the European Union's Horizon 2020 research and innovation program (grant agreement 950533) and from the Israel Science Foundation (grant 1849/19). T.K. is supported by JSPS KAKENHI grant No. 23K13153 and acknowledges support by the Special Postdoctoral Researchers Program at RIKEN. SA acknowledges support from ERC Advanced grant 789410.

This paper makes use of the following ALMA data: ADS/JAO.ALMA#2019.1.01230.S. ALMA is a partnership of ESO (representing its member states), NSF (USA) and NINS

(Japan), together with NRC (Canada), MOST and ASIAA (Taiwan), and KASI (Republic of Korea), in cooperation with the Republic of Chile. The Joint ALMA Observatory is operated by ESO, AUI/NRAO, and NAOJ.

Facilities: Swift, ALMA, NuSTAR.

ORCID iDs

Claudio Ricci https://orcid.org/0000-0001-5231-2645
Chin-Shin Chang https://orcid.org/0000-0001-9910-3234
Taiki Kawamuro https://orcid.org/0000-0002-6808-2052
George C. Privon https://orcid.org/0000-0003-3474-1125
Richard Mushotzky https://orcid.org/0000-0002-7962-5446
Benny Trakhtenbrot https://orcid.org/0000-0002-3683-7297
Ari Laor https://orcid.org/0000-0002-1615-179X
Michael J. Koss https://orcid.org/0000-0002-7998-9581
Krista L. Smith https://orcid.org/0000-0001-5785-7038
Georgios Dimopoulos https://orcid.org/0009-0002-4945-5121
Eduardo Ros https://orcid.org/0000-0001-9503-4892

References

Annuar, A., Gandhi, P., Alexander, D. M., et al. 2015, ApJ, 815, 36
Baumgartner, W. H., Tueller, J., Markwardt, C. B., et al. 2013, ApJS, 207, 19
Begelman, M. C., Blandford, R. D., & Rees, M. J. 1984, RvMP, 56, 255
Behar, E., Baldi, R. D., Laor, A., et al. 2015, MNRAS, 451, 517
Behar, E., Vogel, S., Baldi, R. D., Smith, K. L., & Mushotzky, R. F. 2018, MNRAS, 478, 399
Bianchi, S., Guainazzi, M., & Chiaberge, M. 2006, A&A, 448, 499
Burlon, D., Ajello, M., Greiner, J., et al. 2011, ApJ, 728, 58
Cackett, E. M., Bentz, M. C., & Kara, E. 2021, iSci, 24, 102557
Chartas, G., Kochanek, C. S., Dai, X., Poindexter, S., & Garmire, G. 2009, ApJ, 693, 174
De Marco, B., Ponti, G., Cappi, M., et al. 2013, MNRAS, 431, 2441
Di Matteo, T., Celotti, A., & Fabian, A. C. 1997, MNRAS, 291, 805
Doi, A., & Inoue, Y. 2016, PASJ, 68, 56
Emmanoulopoulos, D., McHardy, I. M., & Papadakis, I. E. 2011, MNRAS, 416, L94
Fabian, A. C., Zoghbi, A., Ross, R. R., et al. 2009, Natur, 459, 540
Galeev, A. A., Rosner, R., & Vaiana, G. S. 1979, ApJ, 229, 318
Guedel, M., & Benz, A. O. 1993, ApJL, 405, L63
Gupta, K. K., Ricci, C., Tortosa, A., et al. 2021, MNRAS, 504, 428
Hildebrand, R. H. 1983, QJRAS, 24, 267
Ichikawa, K., Ricci, C., Ueda, Y., et al. 2017, ApJ, 835, 74
Ichikawa, K., Ricci, C., Ueda, Y., et al. 2019, ApJ, 870, 31
Inoue, Y., & Doi, A. 2014, PASJ, 66, L8
Inoue, Y., & Doi, A. 2018, ApJ, 869, 114
Kara, E., Alston, W. N., Fabian, A. C., et al. 2016, MNRAS, 462, 511
Kawamuro, T., Ricci, C., Imanishi, M., et al. 2022, ApJ, 938, 87
Koss, M., Trakhtenbrot, B., Ricci, C., et al. 2017, ApJ, 850, 74
Koss, M. J., Ricci, C., Trakhtenbrot, B., et al. 2022a, ApJS, 261, 2
Koss, M. J., Trakhtenbrot, B., Ricci, C., et al. 2022b, ApJS, 261, 1
Koss, M. J., Trakhtenbrot, B., Ricci, C., et al. 2022c, ApJS, 261, 6
Koss, M. J., Treister, E., Kakkad, D., et al. 2023, ApJL, 942, L24
Laor, A., & Behar, E. 2008, MNRAS, 390, 847
McHardy, I. M., Gunn, K. F., Uttley, P., & Goad, M. R. 2005, MNRAS, 359, 1469
Mejía-Restrepo, J. E., Trakhtenbrot, B., Koss, M. J., et al. 2022, ApJS, 261, 5
Merloni, A., & Fabian, A. C. 2001a, MNRAS, 328, 958
Merloni, A., & Fabian, A. C. 2001b, MNRAS, 321, 549
Oh, K., Koss, M., Markwardt, C. B., et al. 2018, ApJS, 235, 4
Paltani, S., & Ricci, C. 2017, A&A, 607, A31
Panessa, F., Baldi, R. D., Laor, A., et al. 2019, NatAs, 3, 387
Raginski, I., & Laor, A. 2016, MNRAS, 459, 2082
Ricci, C., Ananna, T. T., Temple, M. J., et al. 2022, ApJ, 938, 67
Ricci, C., & Paltani, S. 2023, ApJ, 945, 55
Ricci, C., Trakhtenbrot, B., Koss, M. J., et al. 2017a, ApJS, 233, 17
Ricci, C., Trakhtenbrot, B., Koss, M. J., et al. 2017b, Natur, 549, 488
Ricci, C., Ueda, Y., Koss, M. J., et al. 2015, ApJL, 815, L13
Risaliti, G., Elvis, M., Fabbiano, G., et al. 2007, ApJL, 659, L111
Smith, K. L., Mushotzky, R. F., Koss, M., et al. 2020, MNRAS, 492, 4216
Smith, K. L., Mushotzky, R. F., Vogel, S., et al. 2016, ApJ, 832, 163
Teng, S. H., Mushotzky, R. F., Sambruna, R. M., Davis, D. S., & Reynolds, C. S. 2011, ApJ, 742, 66
Terashima, Y., & Wilson, A. S. 2003, ApJ, 583, 145
Torres-Albà, N., Marchesi, S., Zhao, X., et al. 2021, ApJ, 922, 252
Uttley, P., Cackett, E. M., Fabian, A. C., Kara, E., & Wilkins, D. R. 2014, A&ARv, 22, 72
Vasudevan, R. V., & Fabian, A. C. 2009, MNRAS, 392, 1124
Wilson, A. S., & Colbert, E. J. M. 1995, ApJ, 438, 62
Zensus, J. A. 1997, ARA&A, 35, 607